

Supercritical Operation of Bearingless Cross-Flow Fan

Ivana Bagaric ^{1,*} , Daniel Steinert ², Thomas Nussbaumer ²  and Johann W. Kolar ¹¹ Power Electronic Systems Laboratory, ETH Zurich, 8092 Zurich, Switzerland; kolar@lem.ee.ethz.ch² Levitronix GmbH, 8048 Zurich, Switzerland

* Correspondence: bagaric@lem.ee.ethz.ch

Abstract: This paper presents a decoupled bearingless cross-flow fan (CFF) that operates at a supercritical speed, thereby increasing the maximum achievable rotational speed and fluid dynamic power. In magnetically levitated CFF rotors, the rotational speed and fan performance are limited by the bending resonance frequency. This is primarily defined by the low mechanical bending stiffness of the CFF blades, which are optimised for fluid dynamic performance, and the heavy rotor magnets on both rotor sides, which add significant mass but a minimal contribution to the overall rotor stiffness. This results in detrimental deformations of the CFF blades in the vicinity of the rotor bending resonance frequency; hence, the CFF is speed-limited to subcritical rotational speeds. The novel CFF rotor presented in this study features additional mechanical decoupling elements with low bending stiffness between the fan blades and the rotor magnets. Thus, the unbalance forces primarily deform the soft decoupling elements, which enables them to pass resonances without CFF blade damage and allows rotor operation in the supercritical speed region due to the self-centring effect of the rotor. The effects of the novel rotor design on the rotor dynamic behaviour are investigated by means of a mass-spring-damper model. The influence of different decoupling elements on the magnetic bearing is experimentally tested and evaluated, from which an optimised decoupled CFF rotor is derived. The final prototype enables a stable operation at 7000 rpm in the supercritical speed region. This corresponds to a rotational speed increase of 40%, resulting in a 28 % higher, validated fluid flow and a 100 % higher static pressure compared to the previously presented bearingless CFF without decoupling elements.

Keywords: bearingless motors; cross-flow-fan; rotor dynamics; rotor decoupling; resonance frequency; supercritical speed



Citation: Bagaric, I.; Steinert, D.; Nussbaumer, T.; Kolar, J.W. Supercritical Operation of Bearingless Cross-Flow Fan. *Machines* **2024**, *12*, 223. <https://doi.org/10.3390/machines12040223>

Academic Editor: Dan Zhang

Received: 29 February 2024

Revised: 22 March 2024

Accepted: 25 March 2024

Published: 27 March 2024



Copyright: © 2024 by the authors. Licensee MDPI, Basel, Switzerland. This article is an open access article distributed under the terms and conditions of the Creative Commons Attribution (CC BY) license (<https://creativecommons.org/licenses/by/4.0/>).

1. Introduction

Cross-flow fans (CFFs) installed in the semiconductor industry are exposed to harsh environmental conditions due to toxic and corrosive gases and are subject to stringent standards. No wear, friction or contamination, and a rotor inside a hermetically sealed process chamber are crucial and lead to the highest performance requirements for the implemented drives. Bearingless motors enable wear-free, practically maintenance-free, and continuous operation of CFFs under these extreme conditions. In [1], the authors presented the bearingless high-speed CFF for applications in deep ultraviolet (DUV) excimer laser, which are commonly used as the light source in industrial lithography systems [2]. The fluid dynamic performance of the CFF is an important factor that limits the gas exchange rate of the lasers in a given, constrained installation space of complex manufacturing devices. Increasing the CFF rotational speed and therefore the fluid performance is a key enabler for improving the laser performance, the scanning speed of lithography systems, and finally, the chip throughput [3–6]. The maximum achievable rotational speed of current bearingless CFFs is restricted by the plastic deformation of the CFF rotor at the critical bending resonance frequency. The operation is therefore limited to subcritical speeds. This paper presents a bearingless CFF rotor, which is operated supercritically to increase the fluid dynamic performance. The CFF rotor features additional mechanical elements with low stiffness

(hereafter referred to as “decoupling elements”), which connect the rotor magnets and the CFF blades according to Figure 1. The influence of the decoupling elements on the rotor dynamic behaviour (vibration modes) is examined by a mass-spring-damper model and the influence on the magnetic bearing is tested with different prototypes. Additionally, the effects on the CFF’s fluid dynamic performance are evaluated.

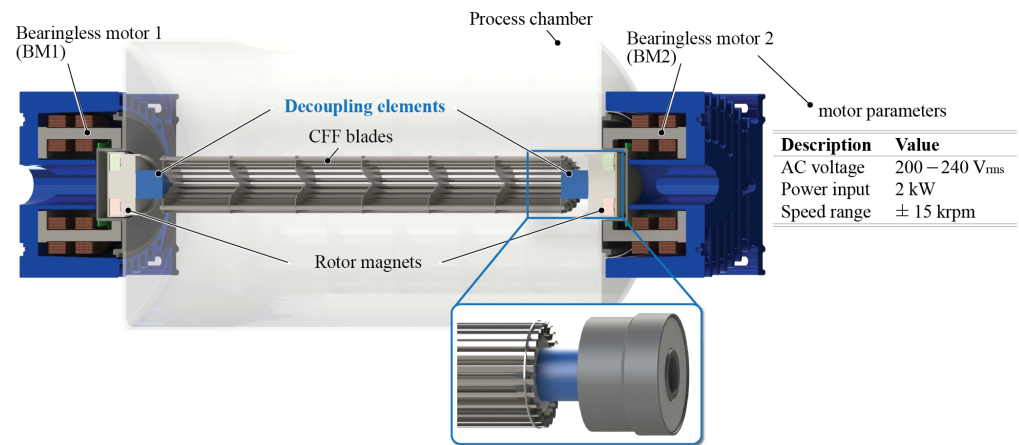


Figure 1. Schematic cross-sectional view of the bearingless CFF system in a hermetically sealed process chamber. The CFF rotor consists of CFF blades, which are decoupled from the rotor magnets by decoupling elements. By adding components with low mechanical stiffness, i.e., $k_{dE} < k_{CFF\text{blades}}$, the rotor dynamical behaviour is influenced such that the resonance frequency, which bends the CFF blades, is shifted to higher rotational speeds.

CFF rotors have a distinctive large length-to-diameter ratio and consist of several thin blades arranged in a circular manner to achieve the optimal fluid dynamic performance [7–9]. The long and thin blades result in a low mechanical bending stiffness. Consequently, the CFF rotor plastically deforms under the unbalance forces, which increase quadratically with the rotational speed, at the critical bending resonance frequency. The use of magnetic bearings amplifies this problem due to the rotor magnets on both ends of the CFF rotor, which add significant mass but minimal contribution to the overall rotor bending stiffness. The CFF rotor presented in [1] consists of two rotor magnets, which are rigidly mounted to the CFF blades as depicted in Figure 2a. The maximum achievable speed is limited by the bending resonance frequency. The low bending stiffness of the CFF blades causes plastic deformation of the blades near the bending resonance frequency, which prevents its surpassing, as shown in Figure 2a with $\omega_{2,CFF_{fix}}$. Thus, the CFF is limited to subcritical operation.

In the literature, different control approaches for the active magnetic bearing system to dampen, pass or eliminate resonance frequencies are proposed [10–23]. Complex position control methods are presented to pass the bending resonance frequency of a flexible test rotor. However, these methods consider massive shafts and Jeffcott rotors with mass distributions and bending stiffnesses that are not comparable to the CFF rotor, of which the mechanical design is restricted by the fluid dynamical requirements. Therefore, the proposed control algorithms are not directly applicable to the problem at hand.

In this paper, however, a rotor design approach is explored to shift the CFF’s critical resonance frequencies and rotor bending to higher rotational speeds. Additional mechanical elements with a low stiffness decouple the CFF blades from the rotor magnets. The vibration behaviour is influenced such that an additional, third resonance frequency occurs as visualised in Figure 2b. The decoupling elements are deformed under the unbalance forces at the first two resonance frequencies $\omega_{1,CFF_{dE}}$ and $\omega_{2,CFF_{dE}}$, which results in a deflection and small, non-plastic deformation of the CFF blades. The two-mode shapes differ in the phase shift between rotor magnets and the CFF rotor. The region above the first two resonance frequencies is referred to as the supercritical region since the CFF rotor centres itself with respect to the rotational axis [24,25]. The third resonance frequency,

$\omega_{3,\text{CFF}_{\text{dE}}}$, is characterised by the detrimental bending of the CFF blades, similar to the second resonance frequency of the non-decoupled CFF, which again leads to plastic deformation of the CFF blades. However, $\omega_{3,\text{CFF}_{\text{dE}}}$ is shifted to higher frequencies than $\omega_{2,\text{CFF}_{\text{fix}}}$ of the non-decoupled rotor. Hence, the new rotational speed limit can be increased.

The design of the multi-component rotor is critical. The decoupling elements must have a low enough mechanical stiffness to enable effective mechanical decoupling and therefore prevent the bending of the blades. But the stiffness cannot be too low such that the fluid dynamic forces acting on the rotor lead to high deflections and instabilities. Furthermore, the magnetic bearing must be able to withstand the forces that result from passing through the resonance frequencies $\omega_{1,\text{CFF}_{\text{dE}}}$ and $\omega_{2,\text{CFF}_{\text{dE}}}$.

This paper aims to address these challenges by first modelling the bearingless CFF rotor with a mass-spring-damper model in Section 2, to analyse the influence of the introduced decoupling element. Various decoupling elements are then experimentally tested, to evaluate their influence on the magnetic bearing and compared with the mass-spring-damper model in Section 3. Finally, the fluid dynamic performance of the CFF rotor with the optimal decoupling element is investigated in Section 4.

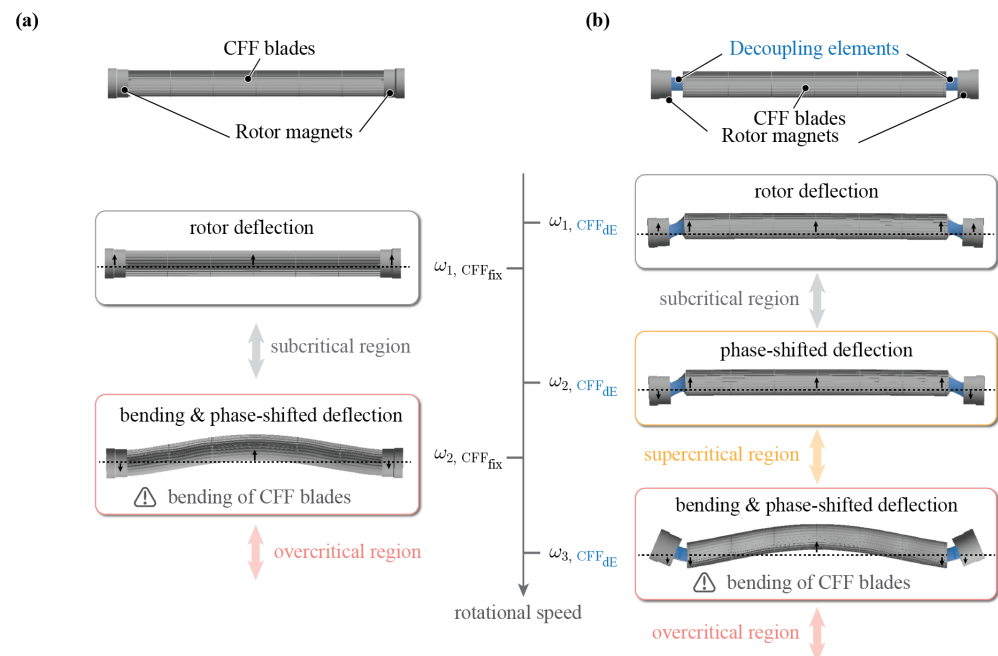


Figure 2. Designs of bearingless CFF rotors: (a) The rotor magnets are directly mounted to the CFF blades (CFF_{fix}), causing plastic deformation at the first critical bending resonance. This limits the maximum achievable rotational speed. (b) The CFF blades are separated from the magnets by additional series elastic elements with low mechanical stiffness (CFF_{dE}). This enables the passing of the first and second bending resonance frequency and shifts the critical bending resonance $\omega_{3,\text{CFF}_{\text{dE}}}$ to higher rotational speeds.

2. Modelling of CFF Resonance Frequencies

The goal of this section is to gain an understanding of the vibration modes of bearingless CFF rotors with and without decoupling elements by means of a mass-spring-damper (mkd)-model. The focus lies on the comparison of the resonance frequencies and mode shapes of CFF rotors with rigidly mounted rotor magnets to the newly introduced, decoupled rotors, particularly to investigate the modes associated with the bending of the CFF blades, since these are speed and performance-limiting. The influence of the decoupling element stiffness is investigated and the effect of shifting the critical bending resonance frequency to higher frequencies explained.

2.1. *mkd*-Model of Bearingless CFF Rotor

The bearingless CFF rotor is modelled using *mkd*-elements as shown in Figure 3. The rotor is assumed symmetrical; thus, only symmetrical vibration modes are studied. The rotor magnets with mass m_B are coupled to the fixed reference frame via the magnetic bearing, which is modelled by the stiffness k_B and damping value d_B . The parameters k_B and d_B can be influenced by the PD position control parameters of the magnetic bearing according to

$$k_B = P \cdot k_i - k_s \quad (1)$$

and

$$d_B = D \cdot k_i \quad (2)$$

where P is the position-proportional and D the velocity-proportional feedback element of the PD control, k_i the force/current and k_s the force/displacement constant of the drive [25]. The CFF blades are represented in a simplified manner with a measured mass m_{CFF} , bending stiffness k_{CFF} and internal damping $d_{i,\text{CFF}}$, while $d_{i,\text{CFF}} \ll d_B$. The mass of the CFF blades is modelled using three mass elements to represent the connection between the rotor magnets and blades as well as to clearly characterise vibration modes leading to rotor bending. The decoupling element, connecting the rotor magnets and CFF blades, is modelled as a spring with stiffness k_{dE} . Its mass and internal damping are assumed to be negligible. The systems' mass unbalance is modelled such that it is concentrated in the CFF centre mass element and that it is created by the small offset ϵ . It denotes the offset of the mass centre from the axis of rotation, which only influences the resonance amplitude and is set to a finite small value for this analysis.

Thus, the following equations of motion are obtained for the modelled CFF system

$$\mathbf{M} \begin{Bmatrix} \ddot{x}_B \\ \ddot{x}_{\text{CFF},e} \\ \ddot{x}_{\text{CFF},c} \end{Bmatrix} + \mathbf{D} \begin{Bmatrix} \dot{x}_B \\ \dot{x}_{\text{CFF},e} \\ \dot{x}_{\text{CFF},c} \end{Bmatrix} + \mathbf{K} \begin{Bmatrix} x_B \\ x_{\text{CFF},e} \\ x_{\text{CFF},c} \end{Bmatrix} = \begin{Bmatrix} 0 \\ 0 \\ F_u(t)/2 \end{Bmatrix}. \quad (3)$$

This results in the unbalance force excitation

$$F_u(t) = m_{\text{CFF}}/4 \cdot \epsilon \cdot \omega^2 e^{j\omega t}, \quad (4)$$

with ϵ being the mass eccentricity rotating at frequency ω [26–32]. The mass matrix \mathbf{M} is defined as

$$\mathbf{M} = \begin{bmatrix} m_B & 0 & 0 \\ 0 & m_{\text{CFF}}/4 & 0 \\ 0 & 0 & m_{\text{CFF}}/4 \end{bmatrix}, \quad (5)$$

the damping matrix \mathbf{D} as

$$\mathbf{D} = \begin{bmatrix} d_B & 0 & 0 \\ 0 & d_{i,\text{CFF}} & -d_{i,\text{CFF}} \\ 0 & -d_{i,\text{CFF}} & d_{i,\text{CFF}} \end{bmatrix} \quad (6)$$

and stiffness matrix \mathbf{K} as

$$\mathbf{K} = \begin{bmatrix} k_{\text{dE}} + k_B & -k_{\text{dE}} & 0 \\ -k_{\text{dE}} & k_{\text{CFF}} + k_{\text{dE}} & -k_{\text{CFF}} \\ 0 & -k_{\text{CFF}} & k_{\text{CFF}} \end{bmatrix}. \quad (7)$$

To simulate the CFF rotor with rigidly mounted rotor magnets, the spring constant of the decoupling element can be set to $k_{\text{dE}} \rightarrow \infty$. Alternatively, for a decoupled CFF rotor, k_{dE} is set to a finite, variable value. An unbalance force F_u is then applied and the following amplitudes are evaluated: magnetic bearing deflection \hat{x}_B , the CFF blades' edge deflection $\hat{x}_{\text{CFF},e}$ and CFF blades' centre deflection $\hat{x}_{\text{CFF},c}$.

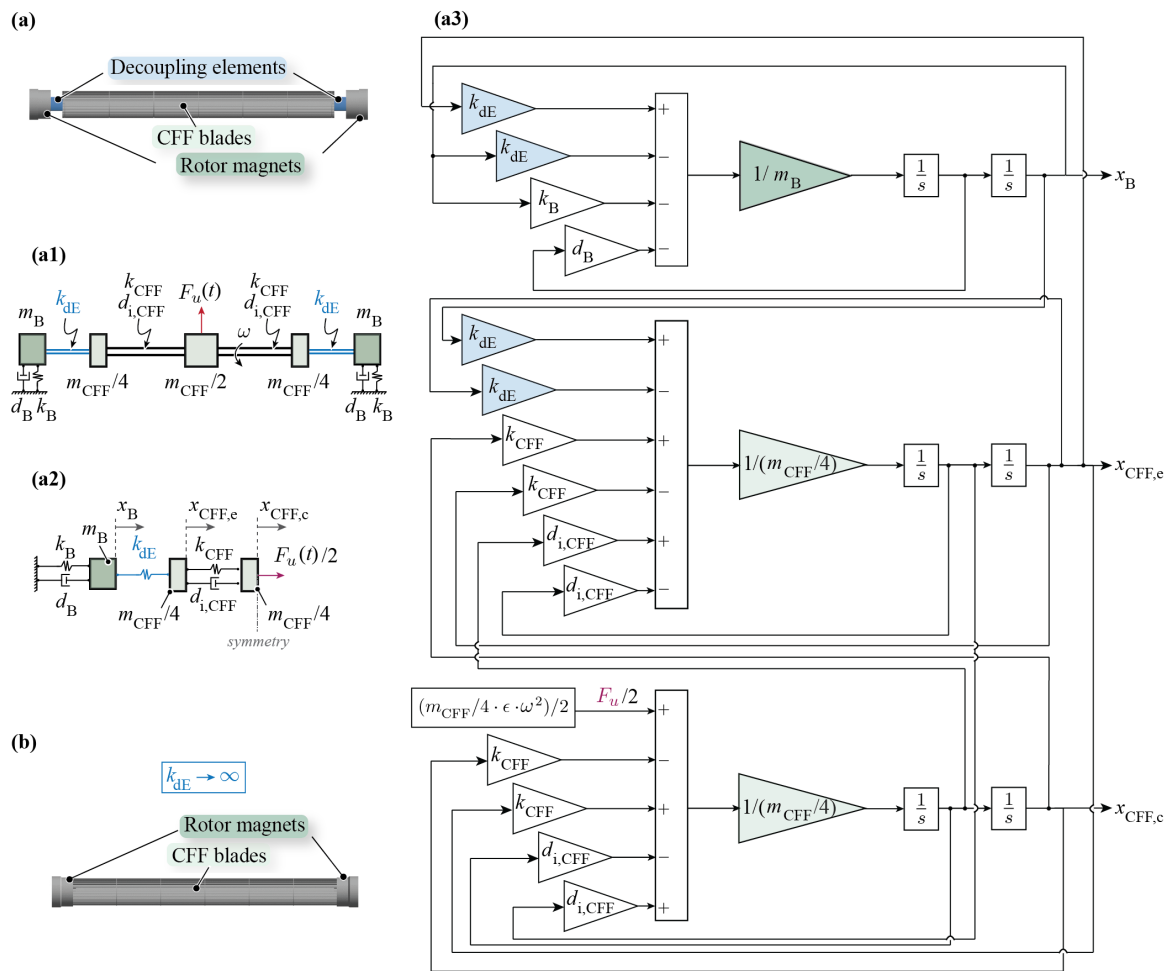


Figure 3. Models of bearingless CFF rotors. (a) The decoupled CFF rotor is shown, where (a1) presents the mechanical and (a2) the simulation *mkd*-model including elements for the magnetic bearing (k_B , d_B), CFF blades (k_{CFF} , $d_{i,CFF}$, m_{CFF}) and decoupling element (k_{dE}), while (a3) shows the algorithm scheme of the implemented simulation model. (b) The CFF rotor with rigidly mounted rotor magnets, which is simulated with $k_{dE} \rightarrow \infty$.

2.2. Unbalance Response of CFF with Rigidly Mounted Rotor Magnets

The simulated resonance frequencies are evaluated with respect to the ratio between the magnetic bearing stiffness k_B and CFF blades stiffness k_{CFF} and the results shown in Figure 4a. In general, the case $k_B/k_{CFF} \rightarrow 0$ represents a free-free supported rotor ($k_B \rightarrow 0$), with ω_1 being the rigid body mode frequency that approaches 0 and ω_2 the free-free resonating rotor, i.e., the bending resonance frequency. For the other extreme edge case of $k_{CFF}/k_B \rightarrow 0$ the bearing is assumed to be rigid ($k_B \rightarrow \infty$). The bending resonance frequency corresponds to ω_1 while $\omega_2 \rightarrow \infty$ represents the resonance of the rotor magnet masses m_B on the magnetic bearing, which is virtually uninfluenced by the blades' stiffness k_{CFF} .

The parameters of the rigid CFF rotor listed in Figure 4b are applied to the *mkd*-model, resulting in the rigid body mode at $\omega_1 = 1920$ rpm and the bending resonance mode at $\omega_2 = 6130$ rpm.

The mode shape of ω_1 is illustrated in Figure 4d, which represents the resonance frequency of the magnetic bearing, i.e., the rigid body mode, where the rotor would deflect from its rotational axis without bending. The rigid body mode does not pose a problem for the operation of the CFF due to the implementation of a force-rejection algorithm in the position controller of the drive, which prevents the unbalance force from exciting this mode [1].

The mode shape of ω_2 depicts the bending of the CFF blades. The CFF blades with heavy rotor magnets mounted on each end can lead to displacements big enough to cause plastic deformation of the CFF blades. This results in permanent damage of the rotor, which strictly limits the directly coupled CFF rotor to subcritical use below ω_2 .

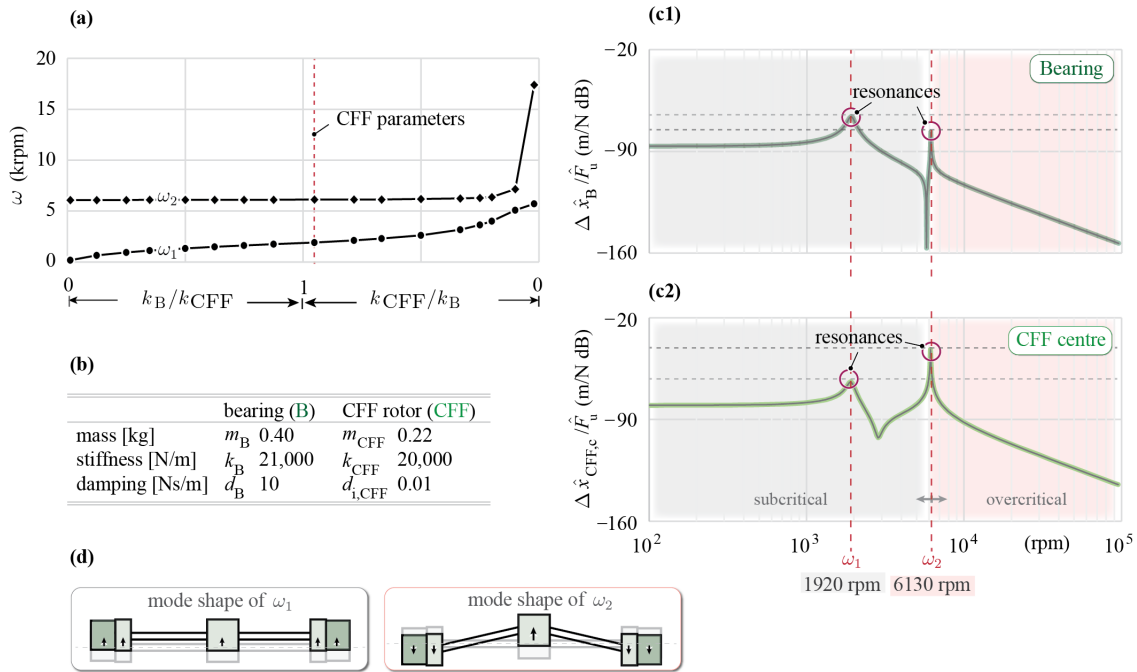


Figure 4. Unbalance response of CFF_{fix} : (a) From the rigidly mounted CFF *mkd*-model ($k_{dE} \rightarrow \infty$) resulting systems' resonance frequencies ω_1 and ω_2 depending on the stiffness ratio between the magnetic bearing k_B and CFF blades stiffness k_{CFF} . (b) *mkd*-model parameters of the CFF rotor. Unbalance force response of the rotor to an unbalance force excitation $F_u(t)$ evaluated at (c1) the magnetic bearing \hat{x}_B and (c2) CFF centre $\hat{x}_{CFF,c}$. The bending mode ω_2 is determined at 6130 rpm. (d) Conceptual drawings of the mode shapes show the bending of the CFF blades at ω_2 , which is the limiting factor for high-speed operation.

2.3. Unbalance Response of CFF with Decoupled Rotor Magnets

For the CFF rotor with mechanically decoupled rotor magnets, the resonance frequencies are evaluated depending on the ratio between the decoupling element stiffness k_{dE} and CFF blades stiffness k_{CFF} . For the simulation, the magnetic bearing stiffness k_B , which according to Equation (1) depends on the force/current and force/displacement constants, defined by the motor topology, and the variable position control parameter P , is set to a fixed value, which results in stable motor operation.

The system response is shown in Figure 5a and the measured CFF rotor parameters are listed in Figure 5b. The stiffness ratio $k_{CFF}/k_{dE} \rightarrow 0$ represents the case $k_{dE} \rightarrow \infty$, which is again the rigidly mounted CFF rotor with $\omega_1 = 1920$ rpm, $\omega_2 = 6130$ rpm and $\omega_3 \rightarrow \infty$ from Section 2.2.

To simulate the decoupling between CFF blades and rotor magnets, the stiffness ratio of $k_{dE}/k_{CFF} = 0.5$ is applied to the *mkd*-model. The amplitude and phase of deflection of an unbalance excitation to this system are then evaluated at the magnetic bearing \hat{x}_B , the CFF blades edge $\hat{x}_{CFF,e}$ as well as centre $\hat{x}_{CFF,c}$ and result in mode shapes of Figure 5d.

The simulation results reveal, that the resonance frequencies of $\omega_1 = 1770$ rpm and $\omega_2 = 3270$ rpm shift downwards, compared to the resonance frequencies from the CFF rotor from Section 2.2.

At ω_1 , the rotor magnets and CFF blades deflect (in phase) from their initial position, whereby the CFF blades remain almost undeformed throughout their length. The mode shape of ω_2 differs in the phase-shift between the deflection of the rotor magnets and CFF

blades. At these rotational speeds, the unbalance forces cause high elastic deformation of the decoupling elements and much lower elastic deformation of the CFF blades, since the decoupling elements possess a lower mechanical stiffness ($k_{dE} < k_{CFF}$). Hence, the critical resonance frequencies ω_1 and ω_2 can be passed. The speed range above these frequencies is considered supercritical, since the CFF rotor self-centres and allows a stable operation up to the third resonance frequency.

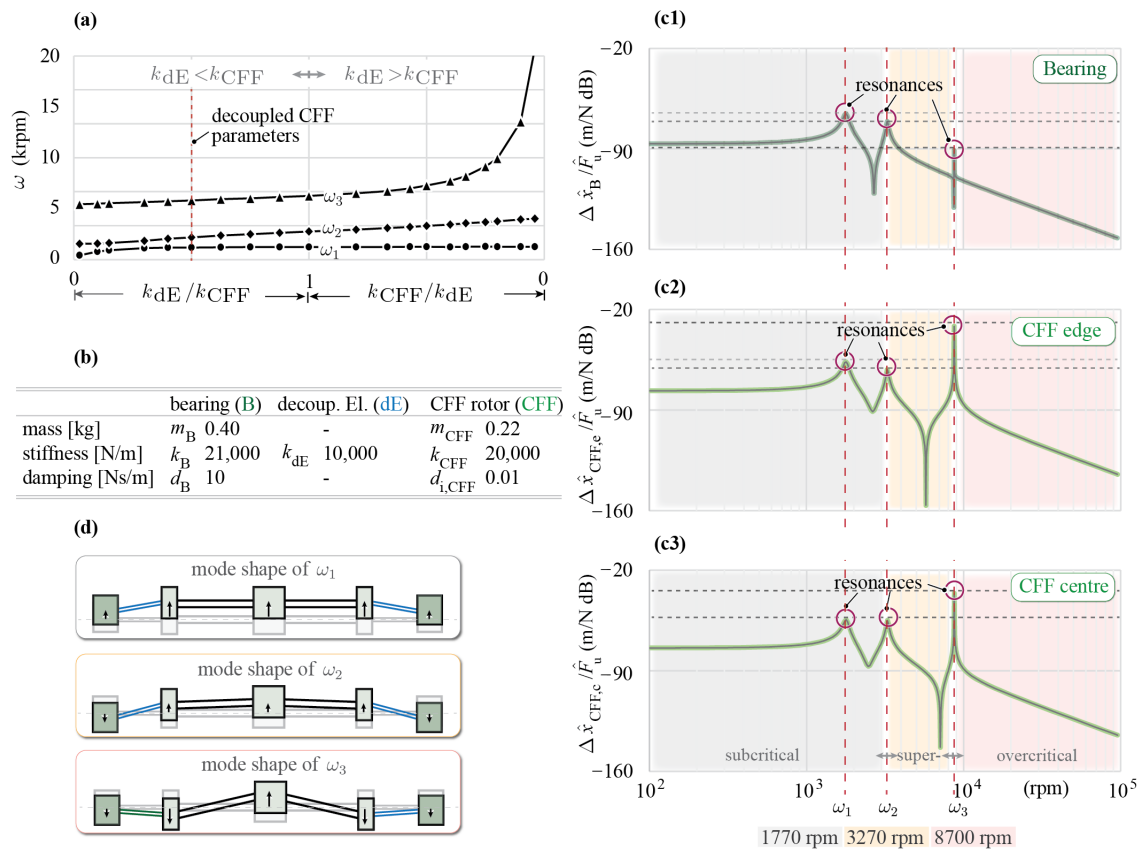


Figure 5. Unbalance response of CFF_{dE}. (a) From the decoupled CFF *mkd*-model resulting systems' resonance frequencies ω_1 , ω_2 and ω_3 depending on the stiffness ratio between the decoupling element stiffness k_{dE} and the CFF blades stiffness k_{CFF} . (b) The *mkd*-model parameters of the CFF rotor with decoupling elements. Unbalance force response of the rotor to an unbalance force excitation $F_u(t)$ evaluated (c1) at the magnetic bearing \hat{x}_B , (c2) CFF edge $\hat{x}_{CFF,e}$ and (c3) CFF centre \hat{x}_{CFF} . The resonance frequency at which the CFF blades bend is determined at 8700 rpm. (d) Conceptual drawings of the mode shapes show the bending of the CFF blades at ω_3 , which is the limiting factor for high-speed operation.

The third resonance frequency ω_3 occurs at 8700 rpm and is associated with the detrimental bending of the CFF blades. It is mainly driven by the stiffness k_{CFF} , which cannot be further modified than what the fluid dynamic design requirements to the blade geometry allow for. Since plastic deformation only occurs when approaching ω_3 , the new speed limit is therefore increased by 42% compared to ω_2 of the rotor with rigidly mounted rotor magnets.

3. Experimental Investigation of Decoupling Elements

The experimental investigation is conducted for different decoupling elements between the CFF blades and the rotor magnets, to examine their influence on the magnetic bearing, which can only compensate for forces and allow displacements to a limited extent. The aim is to determine with which decoupling element the rotor can be operated at the highest rotational speeds. Moreover, the performed rotor dynamic measurements are

compared with the simulation results. These measurements are conducted without the influence of any fluid dynamic loads; therefore, the CFF blades are covered. The rotor magnet displacements in the magnetic bearing are measured using built-in sensors in the bearingless motor 1 (BM1) and 2 (BM2). For the CFF blade displacements $\hat{x}_{\text{CFF},e}$ and $\hat{x}_{\text{CFF},c}$, laser-based distance sensors S1, S2, and S3 are employed to verify the expected mode shapes.

3.1. Influence of the Decoupling Elements on Resonance Frequencies

Seven different decoupling elements are characterised and tested, which leads to the parameters and measured resonance frequencies summarised in Table 1. The respective bending stiffnesses $k_{\text{dE},i}$ are determined by a force-displacement measurement. All decoupling elements consist of the same rubber material and solely vary in their diameter and length.

Table 1. Characteristic parameters and measured resonance frequencies of the tested decoupling elements dE₁ to dE₇.

	i (—)	$k_{\text{dE},i}$ (N/mm)	$m_{\text{dE},i}$ (g)	$\frac{k_{\text{dE},i}}{k_{\text{CFF}}}$ (—)	$\frac{k_{\text{dE},i}}{k_{\text{CFF}}} \frac{m_{\text{CFF}}/4}{m_{\text{dE},i}}$ (—)	$\omega_{1,\text{dE},i}$ (rpm)	$\omega_{2,\text{dE},i}$ (rpm)	$\omega_{3,\text{dE},i}$ (rpm)
(a)	—	—	—	—	—	—	5800	—
(b)	1	16	35	0.80	1.26	3000	6100	—
(c)	2	12.5	51	0.63	0.67	2300	4600	—
(d)	3	10.5	94	0.53	0.31	1900	3500	7400
(e)	4	9.4	60	0.47	0.43	1900	3700	8400
(f)	5	9	43	0.45	0.58	2000	4300	8300
(g)	6	4.9	37	0.25	0.36	1700	3600	8000
(h)	7	4.4	54	0.22	0.22	1400	2800	7600

The measured radial rotor displacements in the magnetic bearing for the CFF with rigidly mounted rotor magnets are shown in Figure 6a and serve as a reference measurement. The rigid body mode does not pose a problem for the magnetic bearing. However, a rapidly increasing radial displacement is measured for BM1 and BM2 when approaching the bending resonance frequency. The unbalance forces lead to a plastic deformation of the CFF blades, therefore it is not possible to pass approximately 5800 rpm.

The rotor dynamic measurements are performed for seven decoupled CFF rotors (Figure 6b–h). Auxiliary touch-down bearings prevent a possible collision between the CFF blades and the static CFF casing walls when passing the first two resonance frequencies.

The aim is to find the decoupling element with the best trade-off between a low enough stiffness k_{dE} , such that the CFF blades do not plastically bend at the second resonance frequency, but a high enough stiffness to shift ω_3 to higher frequencies. Additionally, the mass of the decoupling element should be low to prevent extra mass in the rotor, which leads to a reduction in ω_3 . Furthermore, a high enough k_{dE} is required for the rotor to withstand the fluid dynamic forces created by the CFF blades.

The results from Figure 6b,c show that with decoupling elements dE₁ and dE₂ the target of supercritical operation is not achieved, because their stiffnesses $k_{\text{dE},1}$ and $k_{\text{dE},2}$ are too high. The magnetic bearing is not able to compensate for the forces when approaching the resonance frequencies $\omega_{2,\text{dE},1}$ and $\omega_{2,\text{dE},2}$.

The remaining decoupling elements are successfully operated in the supercritical speed region (Figure 6d–h). It can be seen that decoupling element dE₃ has the lowest resonance frequency ω_3 ; therefore, it reached the lowest maximum speed. This can be justified by its large mass, which is almost 40% higher compared to the second heaviest supercritically operated element.

The measurements further show that decoupling element dE₄ reaches the highest rotational speed. It offers the best trade-off between a low enough stiffness $k_{\text{dE},4}$ to successfully

operate in the supercritical region, and at the same time a high enough stiffness and low mass $m_{dE,4}$, which leads to the highest frequency of ω_3 in this study.

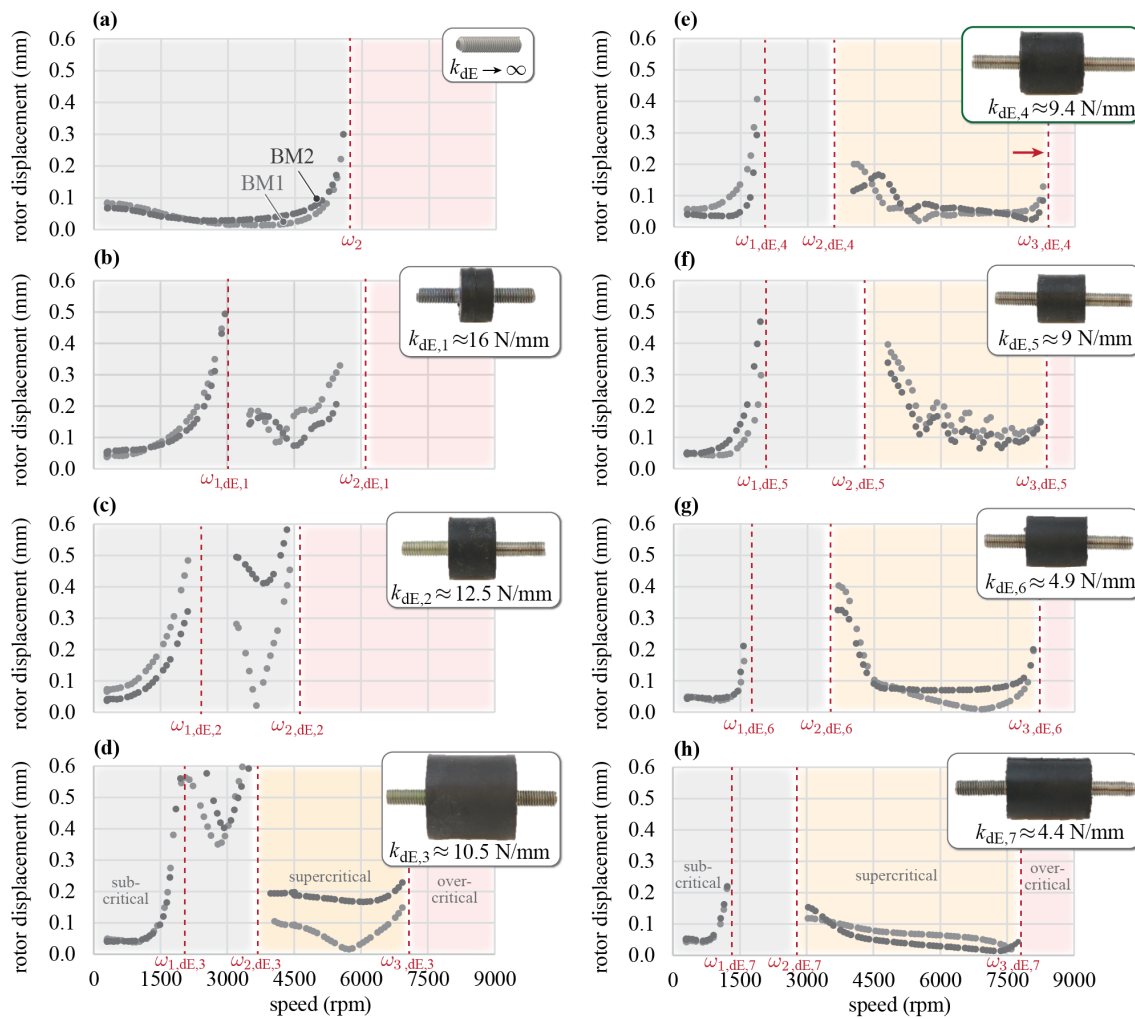


Figure 6. The measured radial rotor displacements in the magnetic bearing are shown in (a) for the CFF rotor with rigidly mounted rotor magnets and in (b–h) for different decoupled CFF rotors. The decoupling element dE_4 from measurement (e) results in the highest speed increase of 45% compared to (a).

3.2. Influence of Decoupling Elements on Mode Shapes

The different mode shapes and the supercritical self-centring effect of the decoupled CFFs are further verified with laser distance measurements on the CFF blades, which are summarised in Figure 7. The results of the CFF with rigidly mounted rotor magnets confirm that the CFF blades start to bend with increasing speed. In the vicinity of the bending resonance frequency, the low bending stiffness of the CFF blades allows the unbalance forces to cause plastic deformation of the blades up to 6 mm (see Figure 7a), thus preventing the passing of the resonance frequency.

The displacements of the CFF rotor with decoupling element dE_4 are measured with the same sensor setup at different rotational speeds. The CFF blades deflect in-phase and out-of-phase with respect to the rotor magnets close to the first and second resonance frequencies, respectively. Additionally, an elastic deformation is measured after the second resonance is passed. The plastic deformation of the CFF blades occurs towards the third resonance frequency ω_3 (see Figure 7(b1)).

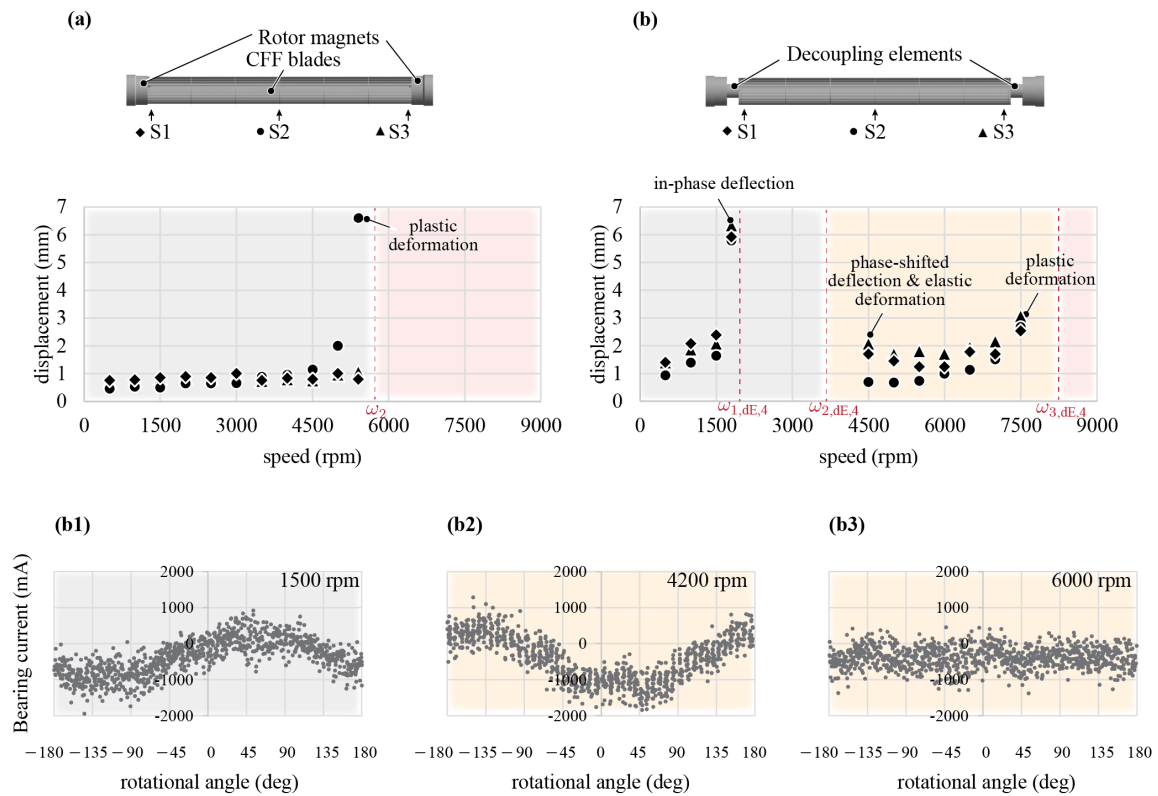


Figure 7. Laser distance sensor measurements of (a) the CFF rotor with rigidly mounted rotor magnets and (b) the CFF rotor with decoupling element dE_4 . Measured bearing currents at (b1) subcritical speed 1500 rpm and (b2) supercritical speeds 4200 rpm and (b3) 6000 rpm, respectively. The 180° phase-shift between the sub- and supercritical bearing currents shows the phase-shifted deflections of mode shape ω_1 and ω_2 . The self-centring effect can be seen from the decrease in the bearing current's amplitude from 4200 rpm to 6000 rpm.

Furthermore, the bearing currents are evaluated at subcritical speeds of 1500 rpm (close to ω_1), at 4200 rpm (shortly after ω_2) and at 6000 rpm (supercritical operation) as seen in Figure 7(b2). The phase shift of 180° between the bearing currents at 1500 rpm and 4200 rpm demonstrates that the force on the magnetic bearing acts in opposing directions. This confirms the phase-shifted deflections of mode shapes ω_1 and ω_2 . From the bearing current at 6000 rpm, a stable supercritical speed operation is detected, clearly showing the self-centring effect of the rotor from ω_2 onwards.

3.3. Comparison and Verification of the *mkd*-Model

The measured resonance frequencies of the rotors fitted with decoupling elements dE_1 to dE_7 are plotted on the simulation results from Section 2.3 with respect to the stiffness ratio of the decoupling element stiffness and the CFF bending stiffness ($k_{dE,i}/k_{CFF}$) in Figure 8a. To eliminate the effect of the decoupling element's mass, which has been neglected in the *mkd*-model, the measured resonance frequencies are plotted with respect to the mass-compensated stiffness ratio $k_{dE,i}/k_{CFF} \cdot \frac{m_{CFF}/4}{m_{dE,i}}$ in Figure 8b. Comparing the experimental data with the simulation results, it can be seen that the resonance frequencies ω_1 , ω_2 and ω_3 increase with increasing decoupling element stiffness $k_{dE,i}$ for both the experimental data and the simulation results. The resonance frequency ω_3 features the lowest slope. The mass compensation method leads to a better fit between the theory and measurements according to Figure 8b. The deviation between simulated and measured resonance frequencies is explained by the approximated model parameters, e.g., the stiffness values have been measured by simplified force-displacement measurements. Additionally, the measured

resonance frequencies have to be estimated in their vicinity, since the rotor cannot be operated in the resonance itself due to resulting mechanical damages.

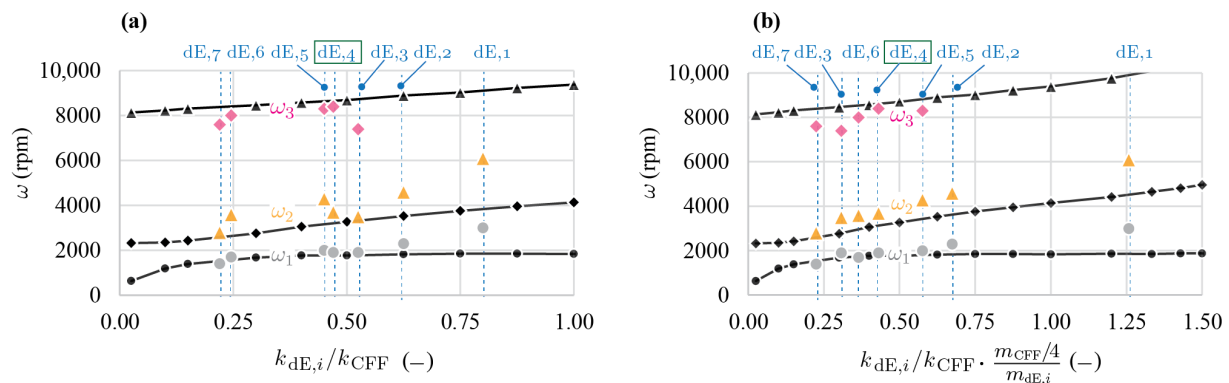


Figure 8. Measured and simulated resonance frequencies of CFF rotors with decoupling element dE_i plotted with respect to the (a) stiffness ratio $k_{dE,i}/k_{CFF}$ and (b) mass-compensated stiffness ratio $k_{dE,i}/k_{CFF} \cdot \frac{m_{CFF}/4}{m_{dE,i}}$.

In summary, this section demonstrates the validity of the rotor dynamical study for CFF rotors with rigidly mounted rotor magnets as well as the introduced, decoupled rotors. A stiffness ratio between k_{dE}/k_{CFF} of 0.47, i.e., dE_4 , leads to the highest achievable rotational speed of the tested decoupling elements. It offers the best trade-off between a “soft” enough decoupling, to be able to penetrate the supercritical region and at the same time a “stiff” enough decoupling element, to shift the third resonance frequency to higher rotational speeds. This leads to an increase in the critical bending resonance frequency from 5800 rpm (rigidly mounted rotor magnets to CFF blades) to 8400 rpm (decoupled rotor with dE_4), which is an increase of 45%. The CFF rotor with decoupling element dE_4 assures a stable operation with low magnetic bearing currents in the supercritical speed region up to 7000 rpm with a safety margin of 17% from the critical resonance frequency ω_3 .

4. Pressure-Flow Characteristics of Decoupled CFF-Rotor

The influence of decoupling the CFF rotor on the fluid dynamic performance is presented in this section. Due to the decoupling elements, the rotor can be operated in the supercritical region of rotational speed up to 7000 rpm. Air flow and pressure measurements in this expanded operation range are performed with the decoupled CFF rotor.

Figure 9a shows the image of the decoupled, bearingless CFF system and Figure 9b the cross-sectional view of the CFF. The rotating CFF blades are surrounded by static casing walls. They are placed close to the rotating fan blades for optimal fluid dynamic performance, but the gap is large enough such that the blades avoid contact with the housing even at the maximum deflection. To prevent a possible collision between the blades and the casing walls when passing the first two resonance frequencies, touch-down bearings are installed in the casing wall on each side of the rotor.

Figure 10a shows the resulting pressure-flow curves of the decoupled, supercritically operated rotor $CFF_{dE,4}$ and the subcritically operated CFF with rigidly mounted rotor magnets, which have been performed on a standardised test setup [1]. The measurements marked in blue show the performance at the speed maximum of 7000 rpm, 17% below the third resonance frequency expected at 8400 rpm. The previously highest rotational speed of the directly coupled CFF at 5000 rpm is marked in grey, which is 14% below the expected bending resonance frequency of 5800 rpm.

Comparing the performance at 5000 rpm of the directly coupled and decoupled CFF, a decrease in flow rate of 10% is noticed (light blue arrow). This can be justified with a reduced active CFF blade length since for the decoupled CFF, auxiliary touch-down

bearings are installed as a safety measure. Therefore, the 40% increase in rotational speed results in an overall increase in fluid flow of 28% and an increase in pressure of 100%.

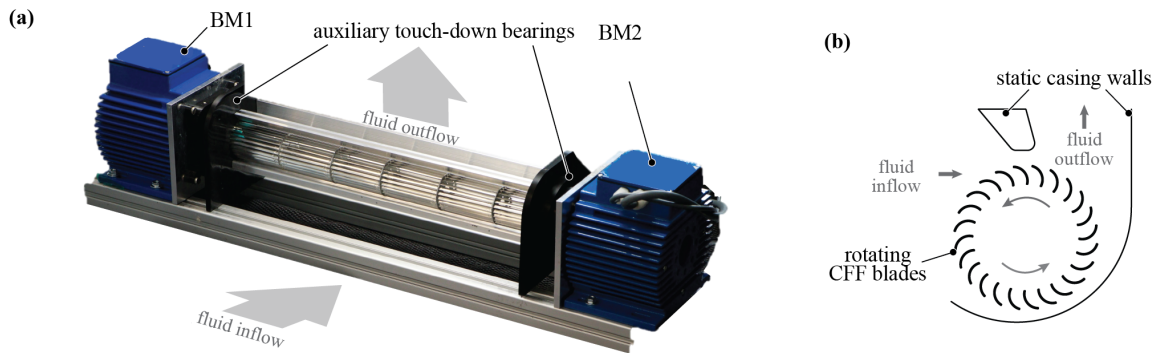


Figure 9. The bearingless CFF for fluid dynamic operation: (a) Image of decoupled, bearingless CFF system including auxiliary touch-down bearings. (b) Schematics of CFF with rotating CFF blades and static casing walls, where the gap between them should be small for an optimised fluid dynamic performance, however, large enough to prevent contact even at the maximum blades’ deflection.

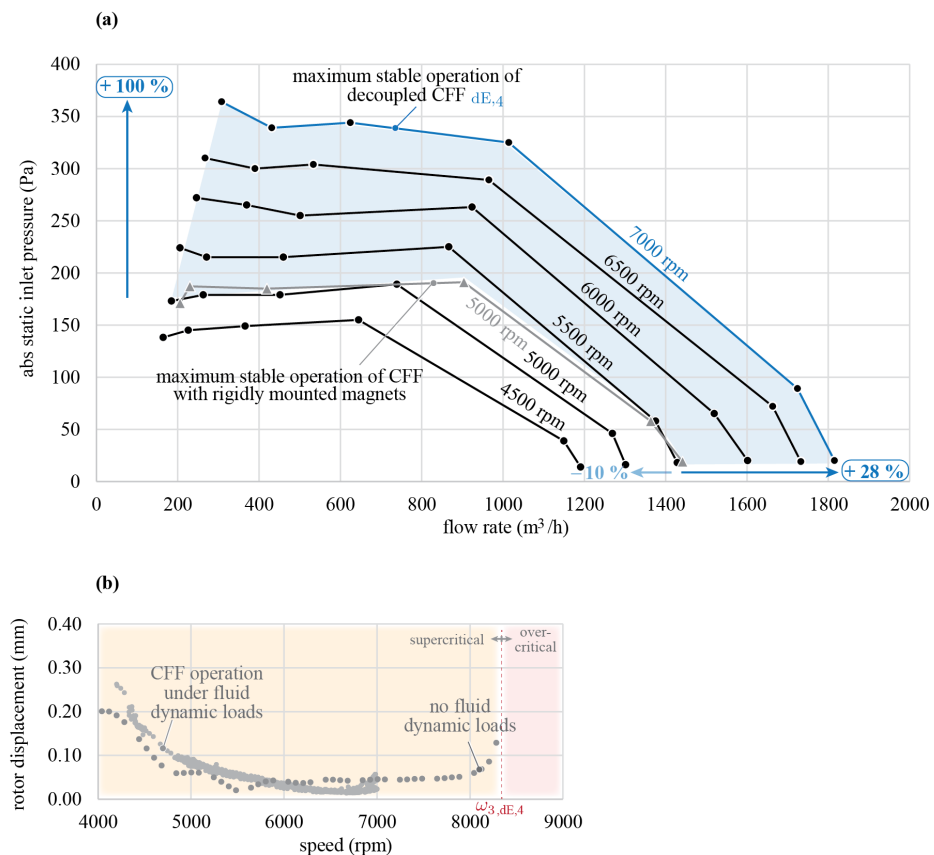


Figure 10. Experimental measurements of bearingless CFF during fluid dynamic operation. (a) Pressure-flow curves for decoupled, supercritically operated rotor CFF_{dE,4} and subcritically operated CFF with rigidly mounted rotor magnets. The maximum achieved performance is marked in blue for the decoupled and in grey for the coupled rotor, respectively. (b) Measured radial rotor displacements in the magnetic bearing of the magnets of BM1 for CFF_{dE,4} under fluid dynamic loads and without any fluid dynamic loads. The fluid dynamic forces only cause small displacements in the magnetic bearing. The CFF is operated up to 7000 rpm with a safety margin of 17% from the critical resonance frequency ω_3 .

Analysing the measured radial rotor displacements in the magnetic bearing of the CFF rotor under fluid dynamic loads (Figure 10b), it can be concluded that a stable operation is possible up to 7000 rpm due to the self-centring effect of supercritical operation and that the fluid dynamic forces only cause small displacements in the magnetic bearing.

5. Discussion and Conclusions

The presented method of decoupling the rotor magnets of bearingless CFFs with mechanical elements of lower bending stiffness compared to the CFF blades, results in an increase in rotational speed and fluid dynamical performance. It is shown, that the blade damaging resonance is shifted to higher frequencies, enabling higher rotational speeds due to the self-centring effect of the rotor. This results in a 40% speed increase and leads to an increase in fluid flow of 28% and an increase in pressure of 100% compared to the previously presented bearingless CFF without decoupling elements.

To achieve a high-speed and high-performance bearingless CFF, the challenge is to increase the rotational speed with measures, that do not negatively impact the fluid dynamic performance.

Methods to increase the rotors' mechanical stiffness and thus the achievable speed, e.g., through design adaptations such as thicker blades or axial rods for rotor stiffening, mostly result in lower fluid performance. Nevertheless, our approach still allows us to expand the CFF design with measures to increase the CFF blades' stiffness.

To the authors' knowledge, there is no comparable control strategy for bearingless motors to pass the bending resonance frequency without the risk of damaging the CFF blades, especially due to their unique mass distribution and bending stiffness. In comparison, the presented approach shifts the blade damaging resonance frequency to higher rotational speeds, hence ensuring that the rotor does not have to be operated in its vicinity or even to pass it.

In summary, the presented method offers a space-saving, simple yet effective mechanical design approach to increase the bearingless' CFFs fluid dynamic performance.

Author Contributions: Conceptualisation, I.B., D.S. and T.N.; methodology, I.B. and D.S.; investigation and validation, I.B.; writing—original draft preparation, I.B.; writing—review and editing, I.B., D.S., T.N. and J.W.K.; supervision, D.S. and J.W.K.; project administration, J.W.K. All authors have read and agreed to the published version of the manuscript.

Funding: This research was funded by the Swiss Innovation Agency Innosuisse, grant number 46738.1.

Data Availability Statement: Data presented in this study are available on request from the corresponding author. The data are not publicly available due to internal policies of the industry research partner.

Acknowledgments: The authors gratefully thank the Swiss Innovation Agency Innosuisse for their financial support and Levitronix GmbH for their financial, scientific, and technical contributions.

Conflicts of Interest: The authors declare no conflicts of interest.

References

1. Bagaric, I.; Hu, R.; Steinert, D.; Nussbaumer, T.; Kolar, J.W. Comparative Evaluation of High-Speed Bearingless Cross-Flow Fan Designs for Lithography Excimer Lasers. *Machines* **2023**, *11*, 611. [[CrossRef](#)]
2. Basting, D.; Marowsky, G. *Excimer Laser Technology*; Springer: Berlin/Heidelberg, Germany, 2005; ISBN 978-3-642-05749-6.
3. Matsunaga, T.; Enami, T.; Kakizaki, K.; Saito, T.; Tanaka, S.; Nakarai, H.; Inoue, T.; Igarashi, T. Extremely high-NA high-throughput-scanner-compatible 4-kHz KrF excimer laser for DUV lithography. In Proceedings of the 26th Annual International Symposium on Microlithography (SPIE), Santa Clara, CA, USA, 14 September 2001; Volume 4346, pp. 1617–1626. [[CrossRef](#)]
4. Kakizaki, K.; Sasaki, Y.; Inoue, T.; Sakai, Y. High-repetition-rate (6kHz) and long-pulse-duration (50ns) ArF excimer laser for sub-65nm lithography. *Rev. Sci. Instrum.* **2006**, *77*, 035109. [[CrossRef](#)]
5. Tsushima, H.; Katsuumi, H.; Ikeda, H.; Asayama, T.; Kumazaki, T.; Kurosu, A.; Ohta, T.; Kakizaki, K.; Matsunaga, T.; Mizoguchi, H. Extremely long life and low-cost 193nm excimer laser chamber technology for 450mm wafer multipatterning lithography. In Proceedings of the Optical Microlithography XXVII (SPIE), San Jose, CA, USA, 4 April 2014; Volume 9052, pp. 411–418. [[CrossRef](#)]

6. Borisov, V.M.; El'tsov, A.V.; Khristoforov, O.B. High-power, highly stable KrF laser with a pulse repetition rate. *Quantum Electron.* **2015**, *45*, 691–696. [[CrossRef](#)]
7. Zhang, W.; Yuan, J.; Si, Q.; Fu, Y. Investigating the In-Flow Characteristics of Multi-Operation Conditions of Cross-Flow Fan in Air Conditioning Systems. *Processes* **2019**, *7*, 959. [[CrossRef](#)]
8. Zou, T.; Zhan, D.; Hu, X.; Hu, S.; Li, Y. Experimental and numerical study of cross-flow fan in air-conditioner indoor unit. *Int. J. Refrig.* **2022**, *141*, 102–111. [[CrossRef](#)]
9. Cai, X.; Zhang, C.; Wang, B. Numerical Study on Fluid Dynamic Characteristics of a Cross-Flow Fan. *J. Mar. Sci. Eng.* **2023**, *11*, 846. [[CrossRef](#)]
10. Zheng, S.; Han, B.; Wang, Y.; Zhou, J. Optimization of damping compensation for a flexible rotor system with active magnetic bearing considering gyroscopic effect. *IEEE/ASME Trans. Mechatron.* **2014**, *20*, 1130–1137. [[CrossRef](#)]
11. Tang, E.; Fang, J.; Zheng, S.; Jiang, D. Active vibration control of the flexible rotor to pass the first bending critical speed in high energy density magnetically suspended motor. *J. Eng. Gas Turbines Power* **2015**, *137*, 112501. [[CrossRef](#)]
12. Tang, E.; Han, B.; Zhang, Y. Optimum compensator design for the flexible rotor in magnetically suspended motor to pass the first bending critical speed. *IEEE Trans. Ind. Electron.* **2015**, *63*, 343–354. [[CrossRef](#)]
13. Heindel, S.; Becker, F.; Rinderknecht, S. Unbalance and resonance elimination with active bearings on a Jeffcott Rotor. *Mech. Syst. Signal Process.* **2017**, *85*, 339–353. [[CrossRef](#)]
14. Ran, S.; Hu, Y.; Wu, H. Design, modeling, and robust control of the flexible rotor to pass the first bending critical speed with active magnetic bearing. *Adv. Mech. Eng.* **2018**, *10*. [[CrossRef](#)]
15. Ran, S.; Hu, Y.; Wu, H.; Cheng, X. Active vibration control of the flexible high-speed rotor with magnetic bearings via phase compensation to pass critical speed. *J. Low Freq. Noise Vib. Act. Control.* **2019**, *38*, 633–646. [[CrossRef](#)]
16. Zheng, Y.; Mo, N.; Zhou, Y.; Shi, Z. Unbalance compensation and automatic balance of active magnetic bearing rotor system by using iterative learning control. *IEEE Access* **2019**, *7*, 122613–122625. [[CrossRef](#)]
17. Kuppa, S.K.; Lal, M. Dynamic behaviour analysis of coupled rotor active magnetic bearing system in the supercritical frequency range. *Mech. Mach. Theory* **2020**, *152*, 103915. [[CrossRef](#)]
18. Gong, L.; Zhu, C. Vibration suppression for magnetically levitated high-speed motors based on polarity switching tracking filter and disturbance observer. *IEEE Trans. Ind. Electron.* **2020**, *68*, 4667–4678. [[CrossRef](#)]
19. Cui, P.; Du, L.; Zhou, X.; Li, J.; Li, Y.; Wu, Y. Harmonic vibration control of MSCMG based on multisynchronous rotating frame transformation. *IEEE Trans. Ind. Electron.* **2021**, *69*, 1717–1727. [[CrossRef](#)]
20. Zheng, S.; Wang, C. Rotor balancing for magnetically levitated TMPs integrated with vibration self-sensing of magnetic bearings. *IEEE/ASME Trans. Mechatron.* **2021**, *26*, 3031–3039. [[CrossRef](#)]
21. Gallego, G.B.; Rossini, L.; Achtnich, T.; Araujo, D.M.; Perriard, Y. Novel generalized notch filter for harmonic vibration suppression in magnetic bearing systems. *IEEE Trans. Ind. Appl.* **2021**, *57*, 6977–6987. [[CrossRef](#)]
22. Alcorta, R.; Chouvion, B.; Montagnier, O. Dynamics of a non-linear Jeffcott rotor in supercritical regime. *Int. J. Non-Linear Mech.* **2023**, *148*, 104272. [[CrossRef](#)]
23. Xu, H.; Li, J.; Lu, Y.; Li, H. Unbalance Control for High-Speed Active Magnetic Bearing Systems Without Speed Sensors. *IEEE Trans. Transp. Electrification.* **2024**, *1*. [[CrossRef](#)]
24. Li, J.; Chen, P.; Liu, J.; Pan, M.; Chen, Q.; Cui, P. Dynamic Modeling and Self-Centering Effect Analysis of Magnetically Suspended Rotor System. *IEEE Sensors J.* **2023**, *23*, 24271–24278. [[CrossRef](#)]
25. Schweitzer, G.; Maslen, E.H. *Magnetic Bearings*; Springer: Berlin/Heidelberg, Germany, 2009; ISBN 978-3-642-10153-3.
26. Kliem, W.; Pommer, C.; Stoustrup, J. Stability of rotor systems: A complex modelling approach. *Z. Angew. Math. Phys. ZAMP* **1998**, *49*, 644–655. [[CrossRef](#)]
27. Gasch, R.; Nordmann, R.; Pfützner, H. *Rotordynamik*; Springer: Berlin/Heidelberg, Germany, 2006; ISBN 3-540-41240-9.
28. Baumgartner, T.; Kolar, J.W. Multivariable state feedback control of a 500,000-r/min self-bearing permanent-magnet motor. *IEEE/ASME Trans. Mechatron.* **2014**, *20*, 1149–1159. [[CrossRef](#)]
29. Pavlenko, I.V.; Simonovskiy, V.I.; Demianenko, M.M. Dynamic Analysis of Centrifugal Machines Rotors Supported on Ball Bearings by Combined Application of 3D and Beam Finite Element Models. *IOP Conf. Ser. Mater. Sci. Eng.* **2017**, *233*, 012053. [[CrossRef](#)]
30. Ruggiero, A.; D'Amato, R.; Magliano, E.; Kozak, D. Dynamical simulations of a flexible rotor in cylindrical uncavitated and cavitated lubricated journal bearings. *Lubricants* **2018**, *6*, 40. [[CrossRef](#)]
31. Hutterer, M.; Schroedl, M. Stabilization of active magnetic bearing systems in the case of defective sensors. *IEEE/ASME Trans. Mechatron.* **2021**, *27*, 3672–3682. [[CrossRef](#)]
32. Hubmann, E.J.; Weissöfner, F.; Steinert, D.; Nussbaumer, T.; Kolar, J.W. Novel Acoustic Failure Prediction Method for Active Magnetic Bearing Systems. *IEEE/ASME Trans. Mechatron.* **2023**, 1–12. [[CrossRef](#)]

Disclaimer/Publisher's Note: The statements, opinions and data contained in all publications are solely those of the individual author(s) and contributor(s) and not of MDPI and/or the editor(s). MDPI and/or the editor(s) disclaim responsibility for any injury to people or property resulting from any ideas, methods, instructions or products referred to in the content.